Nonlinear Stability of the Classical Nusselt Problem of Film Condensation and Wave Effects

L. Phan

A. Narain
e-mail: narain@mtu.edu

Department of Mechanical Engineering—
Engineering Mechanics,
Michigan Technological University,
Houghton, MI 49931

Accurate steady and unsteady numerical solutions of the full two-dimensional (2D) governing equations for the Nusselt problem (film condensation of quiescent saturated vapor on a vertical wall) are presented and related to known results. The problem, solved accurately up to film Reynolds number of 60 ($\mathrm{Re}_\delta \leqslant 60$)*, establishes various features of the well-known steady solution and reveals the interesting phenomena of stability, instability, and nonlinear wave effects. It is shown that intrinsic flow instabilities cause the wave effects to grow over the well-known experiments-based range of* $\mathrm{Re}_\delta \geqslant 30$*. The wave effects due to film flow's sensitivity to ever-present minuscule transverse vibrations of the condensing surface are also described. The results suggest some ways of choosing wall noise—through suitable actuators—that can enhance or dampen wave fluctuations and thus increase or decrease heat transfer rates over the laminar-to-turbulent transition zone.* [DOI: 10.1115/1.2198249]

1 Introduction

The Nusselt problem [1] of film condensation of quiescent saturated vapor on a vertical wall has been extensively studied—analytically, computationally, and experimentally. For this problem, the state of empirical knowledge with regard to typical wave effects on the heat transfer rates is quite good (see [2]). Despite this, a good understanding of noise effects and instability mechanisms for the flow has been lacking. With the help of first-principles-based computational simulations, this paper explores these issues and presents new results and understanding. Furthermore, compatibility with the well-known results for this problem provides a test of the efficacy of the first-principles-based simulation methodology employed here. This benchmark study, along with some experimental results, also strengthens the confidence in other convergent computational solutions obtained by essentially the same simulation methodology for *internal* condensing flows studied elsewhere [3–5].

The well-known analytical solution [1] of the Nusselt problem was improvised by Rohsenow [6] to account for the effects of the energy convection term. Subsequently, Sparrow and Gregg [7] provided a similarity solution under the assumption of zero interfacial shears. Vapor shear effects were accounted for, by an integral method, in the work of Chen [8], and, by a similarity solution technique, in the work of Koh et al. [9]. Dhir and Lienhard [10] applied/generalized the solution for situations involving varying gravitational inclinations. The computational solution of the steady problem that has been presented in this paper is consistent with the well-known Nusselt solution and its improvements. A good review of the criteria for the range of applicability of the Nusselt solution and its modifications is available in Arnas et al. [11]. More specifically, this paper solves the steady Nusselt problem without making any of the usual approximations for the governing equations and yet yields the solutions which are in a good agreement with the Nusselt solution [1]. The paper also shows that, for steady solutions, it is only the near-interface vapor pressure field (p_2-p_0) that is significantly affected by the presence or absence of surface tension.

The unsteady solution for this problem—after ignoring the restriction based on the continuity of tangential velocities at the interface—has been attempted by Miyara [12]. This work has tried to improvise upon earlier related computational efforts [13] for this problem. But these computational results suffer from the fact that the three different ways of computing interfacial mass flux values (from considerations of the relative velocity of vapor at the interface, the relative velocity of liquid at the interface, and the heat transfer rates across the interface) are not equal to one another. In this regard, the simulation results presented here are accurate and are shown to satisfy this and all the remaining interface conditions.

Wave initiation mechanisms can, in principle, also be understood by linear or nonlinear stability analyses. The linearized stability analyses of Unsal and Thomas [14] and Spindler [15] yield results that are mutually consistent but do not satisfy the well-known experimental results that are associated with laminar-to-turbulence transition over $\mathrm{Re}_\delta \geqslant \mathrm{Re}_\delta|_{\mathrm{Cr}}$ with $\mathrm{Re}_\delta|_{\mathrm{Cr}} \approx 30$. The experimental observance of this laminar-to-turbulent transition is believed to be related to Tollmien-Schlichting-type instability waves [16] that are suitably modified by free surface phenomena and mass transfer across the interface. The paper shows that the instability mechanism for this problem is necessarily a nonlinear phenomenon in time (as opposed to nonlinearities due to the size of the amplitudes alone) and, therefore, cannot be identified by either the linearized stability analyses assumption ([14,15]) or partial nonlinear analyses ([17]) that employ two term expansions in wave number and wave amplitude. This full nonlinear stability analysis presented here does achieve agreement with the reported values of $\mathrm{Re}_\delta|_{\mathrm{Cr}} \approx 30$.

Our results are in basic agreement with the known experimental result that laminar wavy flows occur over a zone for which, approximately, $\mathrm{Re}_\delta \geqslant 30$ (see Re_δ definition in the Nomenclature and Incropera et al. [2]) and that the waves are typically small to nonexistent over a zone for which, approximately, $\mathrm{Re}_\delta \leqslant 30$. Experimentally obtained local heat transfer coefficients for the wavy regime have been proposed by Kutateladze [18], Chun and Seban [19], etc., and are also given in Incropera et al. [2]. The results given here are consistent with the range of heat transfer enhancements that are expected under typical wavy conditions.

Contributed by the Applied Mechanics Division of ASME for publication in the Journal of Applied Mechanics. Manuscript received October 16, 2005; final manuscript received January 26, 2006. Review conducted by T. E. Tezduyar. Discussion on the paper should be addressed to the Editor, Prof. Robert M. McMeeking, Journal of Applied Mechanics, Department of Mechanical and Environmental Engineering, University of California—Santa Barbara, Santa Barbara, CA 93106-5070, and will be accepted until four months after final publication of the paper itself in the ASME Journal of Applied Mechanics.

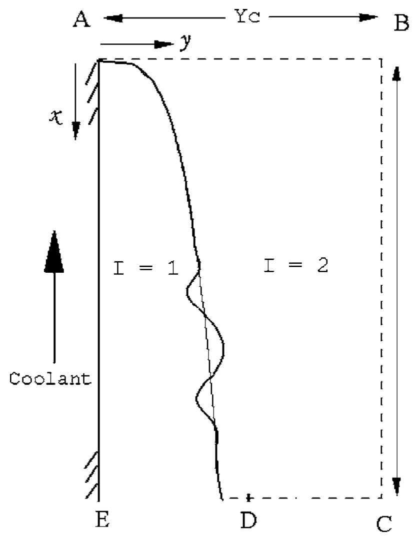

Fig. 1 Cooled vertical plate in a quiescent (far field) vapor flow—geometry used for simulations

Unlike the linearized stability analyses, the accurate simulations reported here also suggest an insignificant role of surface tension on the value of $\mathrm{Re}_\delta|_{\mathrm{cr}} \cong 30$. This is in agreement with experiments for this gravity driven flow but not in agreement with the results based on the linearized stability analyses given in [14,15].

This paper also clearly identifies how significantly wall noise interacts with Tollmien-Schlichting-type growing waves in the wavy laminar regime (i.e., transition to turbulence regime, which is typically characterized by $30 \leq \mathrm{Re}_\delta \leq 1800$). It is shown that wall noise—modeled as a linear superposition of transverse displacement standing waves of different amplitude, frequency, and wavelength—can either diminish or accentuate the wave effects. The enhancement of wave effects can be ensured if one can place suitably chosen noise sources (e.g., actuators) that satisfy a certain resonance condition. This result highlights the fact that knowledge and control of wall noise are important issues in ensuring repeatability of wave effects in the transition-to-turbulence regime.

2 Governing Equations

The liquid and vapor phases in the flow (e.g., see Fig. 1) are denoted by a subscript I: $I=1$ for liquid and $I=2$ for vapor. The fluid properties (density ρ, viscosity μ, specific heat C_p, and thermal conductivity k) with subscript "I" are assumed to take their representative constant values for each phase ($I=1$ or 2). Let $\mathcal{T}_\mathrm{I}$ be the temperature fields, p_I be the pressure fields, $\mathcal{T}_s(p)$ be the saturation temperature of the vapor as a function of local pressure p, Δ be the film thickness, $\dot{m}$ be the local interfacial mass flux, $\mathcal{T}_w(x)$ $[<\mathcal{T}_s(p)]$ be a *known* temperature variation [here $\mathcal{T}_w(x) = \text{constant} = \mathcal{T}_w(0)$] of the cooled bottom plate, and $\mathbf{v}_\mathrm{I} = u_\mathrm{I}\hat{\mathbf{e}}_x + v_\mathrm{I}\hat{\mathbf{e}}_y$ be the velocity fields. As shown in Fig. 1, instead of the original infinite domain ($x \geq 0$ and $y \geq 0$), solutions are only to be obtained over a finite subdomain ($0 \leq x \leq X_c$ and $0 \leq y \leq Y_c$). For convenience, the characteristic length for this problem is chosen to be Y_c, where Y_c is a known numerical multiple of the well known ([1]) physical value of the steady Nusselt film thickness $\Delta_N(x)$ at $x = X_c$. That is, $Y_c \equiv c \cdot \Delta_N(X_c)$, where c is a known number (e.g., $c=47$ for all cases shown here). This makes Y_c a priori known and sufficiently large to capture all the relevant vapor flow. While other choices of characteristic length Y_c are possible [e.g., $Y_c \equiv \Delta_N(X_c)$], this choice is convenient for implementing the computational approach employed here. Furthermore, let the characteristic speed U be the *average* value, at $x = X_c$, of the x component of the liquid speed obtained from the well-known [1] Nusselt solution. That is, $U \equiv g(\rho_1 - \rho_2) \cdot \Delta_N(X_c)^2 / 3\mu_1$. The above choices of characteristic length and speed are used for defining the nondimensional variables whose computationally obtained values are reported in this paper. As needed, this choice is related to other results obtained from other commonly used choices of characteristic length and speed. Let $\mathfrak{g}_x$ and $\mathfrak{g}_y$ be the components of gravity along x and y axes, p_0 be the pressure of the far-field quiescent vapor, $\Delta\mathcal{T} \equiv \mathcal{T}_s(p_0) - \mathcal{T}_w(0)$ be the representative controlling temperature difference between the vapor and the bottom plate, and h_{fg} be the heat of vaporization at saturation temperature $\mathcal{T}_s(p)$. With t representing the physical time, we introduce a new list of fundamental nondimensional variables through the following definitions:

$$\{x, y, \delta, u_I, \dot{m}\} \equiv \left\{ \frac{x}{Y_c}, \frac{y}{Y_c}, \frac{\Delta}{Y_c}, \frac{u_I}{U}, \frac{\dot{m}}{\rho_1 U} \right\}$$

$$\{v_I, \theta_I, \pi_I, t\} \equiv \left\{ \frac{v_I}{U}, \frac{\mathcal{T}_I}{\Delta\mathcal{T}}, \frac{p_I - p_0}{\rho_1 U^2}, \frac{t}{(Y_c/U)} \right\} \tag{1}$$

2.1 Interior Equations. The nondimensional differential forms of mass, momentum (x and y components) and energy equations for flow in the interior of either of the phases are well-known and are given in (A1)–(A4) of the Appendix. The simplified forms that are used in obtaining the Nusselt ([1]) solution are given by (A1) and (A5) of the Appendix.

2.2 Interface Conditions. The nearly exact interface conditions (Delhaye [20]) for condensing flows, with some approximations, are given in Narain et al. [3]—see their Appendix Eqs. (A1)–(A9). Utilizing a superscript "i" for values of the flow variables at the interface given by $\mathcal{H} \equiv y - \Delta(x, t) = 0$, the nondimensionalized forms of the interface conditions are given below.

- The nondimensional form of the requirement of continuity of tangential component of velocities (Eq. (A2) of [3]) becomes:

$$u_2^i = u_1^i - \delta_x (v_2^i - v_1^i) \tag{2}$$

where $\delta_x \equiv \partial\delta/\partial x$.

- The nondimensional form of the normal component of momentum balance at the interface (Eq. (A3) of [3]) becomes:

$$\pi_1^i = \frac{\rho_2}{\rho_1}\pi_2^i - \frac{1}{\mathrm{We}}\left(\frac{\delta_{xx}}{[1+\delta_x^2]^{3/2}} \right) + \dot{m}^2 \left(\frac{\rho_1}{\rho_2} - 1 \right) \tag{3}$$

where $\mathrm{We}^{-1} \equiv \sigma / \rho_1 U^2 Y_c$ and surface tension $\sigma = \sigma(\mathcal{T})$ with $\mathcal{T}$ being the interfacial temperature.

- The tangential component of momentum balance at the interface (Eq. (A4) of [3]) becomes:

$$\left.\frac{\partial u_1}{\partial y}\right|^i = \left.\frac{\mu_2}{\mu_1}\frac{\partial u_2}{\partial y}\right|^i + [t] \tag{4}$$

The term $[t]$ used here is defined by Eq. (A6) of the Appendix.

- The nondimensional forms of non-zero interfacial mass fluxes $\dot{m}_{LK}$ and $\dot{m}_{VK}$ (defined in Eq. (A5) of [3]) impose kinematic constraints on the interfacial values of the liquid and vapor velocity fields and are given by:

$$\dot{m}_{LK} \equiv [u_1^i(\partial\delta/\partial x) - (v_1^i - \partial\delta/\partial t)]/\sqrt{1+(\partial\delta/\partial x)^2} \text{ and}$$

$$\dot{m}_{VK} \equiv (\rho_2/\rho_1)[u_2^i(\partial\delta/\partial x) - (v_2^i - \partial\delta/\partial t)]/\sqrt{1+(\partial\delta/\partial x)^2} \tag{5}$$

- The nondimensional form of nonzero-interfacial mass flux $\dot{m}_{\mathrm{Energy}}$ (as given by Eq. (A6) of [3]) represents the constraint imposed on mass flux by the balance equation for the net energy transfer across the interface, and is given by:

$$\dot{m}_{\rm Energy} \equiv {\rm Ja}/({\rm Re}_1\,{\rm Pr}_1)\{\,\partial\theta_1/\partial n|^i - (k_2/k_1)\,\partial\theta_2/\partial n|^i\} \quad (6)$$

where $\mathrm{Ja} \equiv C_{p1}\Delta\mathcal{T}/h_{fg}^0$ and $h_{fg}^0 \equiv h_{fg}[\mathcal{T}_s(p_o)] \cong h_{fg}[\mathcal{T}_s(p_2^i)]$.

- The interfacial mass balance requires that the net mass flux (in kg/m^2/s) at a point on the interface, as given by Eq. (A7) of [3], be single valued regardless of which physical process is used to obtain it. The nondimensional form of this requirement becomes:

$$\dot{m}_{LK} = \dot{m}_{VK} = \dot{m}_{\rm Energy} \equiv \dot{m} \quad (7)$$

It should be noted that negligible interfacial thermal resistance and equilibrium thermodynamics on either side of the interface are assumed to hold for x values downstream of the origin (i.e., second or third computational cell onward). And hence, as in Nusselt [1] solution and as per discussions leading to Eq. (A8) in [3], no nonequilibrium thermodynamic model for the interfacial mass-flux $\dot{m}$ is needed to obtain a solution.

- The nondimensional thermodynamic restriction on interfacial temperatures (as given by Eq. (A8) in [3]) becomes:

$$\theta_1^i \cong \theta_2^i = \mathcal{T}_s(p_2^i)/\Delta\mathcal{T} \equiv \theta_s(\pi_2^i) \quad (8)$$

Within the vapor domain, for any of the typical refrigerants (such as R113 considered here) changes in absolute pressure relative to the inlet pressure are sufficient to affect vapor motion, but, at the same time, they are too small to affect saturation temperatures. This allows the approximation: $\theta_s(\pi_2^{\rm i}) \cong \theta_s(0)$.

2.3 Boundary Conditions. Since the vapor is stationary at locations far away from the condensate, the appropriate far field vapor boundary conditions are prescribed along lines AB ($\mathscr{x}=0$), BC ($\mathscr{y}=Y_c$), and CD ($\mathscr{x}=X_c$ or $x=x_c=X_c/Y_c$) in Fig. 1. These are:

- $\pi_2(0,y,t)=0$ and $\left.\dfrac{\partial u_2}{\partial x}\right|_{(0,y,t)} = 0$
- $\pi_2(x,1,t)=0$ and $\left.\dfrac{\partial v_2}{\partial y}\right|_{(x,1,t)} = 0$
- $\pi_2(x_c,y,t)=0$ and $\left.\dfrac{\partial u_2}{\partial x}\right|_{(x_c,y,t)} = 0 \quad (9)$

At the condensing surface ($y=0$), we have:

$$u_1(x,0,t) = v_1(x,0,t) = 0 \text{ and } \theta_1(x,0,t) = \theta_w \equiv \mathcal{T}_w/\Delta\mathcal{T} \quad (10)$$

Furthermore, vapor can be assumed to be at uniform saturation temperature—i.e., $\theta_2(x,y,t) \cong \theta_s(0)$ at all locations in the vapor domain. This is reasonable because effects of superheat $\Delta\mathcal{T}_{\rm sup}$ (in the typical 5–10°C range) are verifiably negligible for the typically small values of vapor Jacob number ($\mathrm{Ja}_v \equiv Cp_2\cdot\Delta\mathcal{T}_{\rm sup}/h_{fg}^{\rm o}$) encountered for most vapor flow conditions studied here. The point D at $\mathscr{x}=X_c$ is considered to be slightly but sufficiently above the interface and no exit condition is imposed along ED. However the mass flow over ED—which specifically includes the liquid portion $0 \leqslant y \leqslant \delta(x_c)$—is required to satisfy the overall mass balance for a control volume formed by the bounding surfaces $\mathscr{x}=0$, $\mathscr{x}=X_c$, $\mathscr{y}=0$, and $\mathscr{y}=Y_c$.

2.4 Initial Conditions. The above described *continuum* equations do not model and incorporate various intermolecular forces that are important in determining the time evolution of very thin (10–100 nm) condensate film thickness $\delta(x,t)$. As a result, $t=0$ cannot be chosen to be the time when saturated vapor first comes in contact with and condenses on the dry subcooled $[\mathcal{T}_w(x) < \mathcal{T}_s(p_0)]$ vertical/inclined wall. With the above modeling limitations, the strategy here is to start at a time ($t=0$) for which one has a sufficiently thick *steady* solution of the *continuum* equations (where all of the governing equations clearly apply) and then, from there, one can obtain the natural large time ($t\to\infty$) smooth or wavy (steady/quasi-steady) solutions with the help of the unsteady equations. That is, if $\phi(x,y,t)$ is any variable (such as, $u_{\rm I}$, $v_{\rm I}$, $\pi_{\rm I}$, $\theta_{\rm I}$, etc.), the initial values of ϕ and film thickness $\delta(x,t)$ are given as:

$$\phi(x,y,0) = \phi_{\rm steady}(x,y) \text{ and } \delta(x,0) = \delta_{\rm steady}(x) \quad (11)$$

where $\phi_{\rm steady}$ and $\delta_{\rm steady}$ are the solutions of the governing equations obtained by dropping all time dependencies in Eqs. (2)–(11).

An inspection of all the non-dimensional governing equations, interface conditions, and boundary conditions reveals the fact that the flows considered here are affected by the following set of eight independent non-dimensional parameters:

$$\left\{ \mathrm{Re}_1, \mathrm{Ja}, \mathrm{Fr}_x^{-1}, \mathrm{Fr}_y^{-1}, \frac{\rho_2}{\rho_1}, \frac{\mu_2}{\mu_1}, \mathrm{Pr}_1, \mathrm{We} \right\} \quad (12)$$

where $\mathrm{Re}_1 \equiv \rho_1 U Y_c/\mu_1$ indirectly depends on the physical value of $\mathscr{x}=X_c$.

2.5 Nusselt Formulation/Solution. Besides the assumptions and approximations that lead to the interior equations given in the Appendix—namely (A1) with $I=1$ and (A5), this Nusselt ([1]) formulation for the underlying steady problem assumes: a small slope approximation ($\delta'^2 \ll 1$), negligible surface tension ($\mathrm{We}^{-1} \cong 0$) as well as negligible momentum transfer effects on the right side of Eq. (3), and zero to negligible vapor viscosity. The assumption of negligible vapor viscosity makes continuity of tangential velocity condition in Eq. (2) to become irrelevant. This means that condensate motion is not affected by the equations governing the vapor motion and any constraints arising from the interfacial mass flux $\dot{m}_{VK}$ defined in Eq. (5). As a result, the steady Nusselt formulation requires that (A1) for $I=1$ and (A5) in the Appendix be solved subject to Eqs. (9) and (10) and the following simplified interface conditions:

- $\pi_2^i = 0$ and $\pi_1^i = 0$ as a replacement of Eq. (3)
- $\left.\dfrac{\partial u_1}{\partial y}\right|^i = 0$ as a replacement of Eq. (4)
- $\dot{m}_{LK} = \left[u_1^i \dfrac{d\delta}{dx} - v_1^i \right] = \dfrac{d}{dx}\left[\displaystyle\int_0^{\delta(x)} u_1(x,y)\cdot dy \right]$ as a replacement of Eq. (5)
- $\dot{m}_{\rm Energy} \equiv \mathrm{Ja}/(\mathrm{Re}_1\,\mathrm{Pr}_1)\cdot\ \partial\theta_1/\partial y|^i$ as a replacement of Eq. (6)
- $\dot{m}_{LK} = \dot{m}_{\rm Energy}$ as a replacement of Eqs. (2) and (7)
- $\theta_1^i = \theta_2^i = \theta_s(\pi_2^i)$, i.e., Eq. (8) remains the same $\quad (13)$

The analytical solution of the above Nusselt formulation is known as the Nusselt ([1]) solution and is well known ([2]). This classical solution (see, e.g., [2]) and its principle results are:

$$\Delta(\mathscr{x}) \equiv \Delta_N(\mathscr{x}) \equiv Y_c\delta_N = \left[\frac{4k_1\mu_1\Delta\mathcal{T}\mathscr{x}}{g\rho_1(\rho_1-\rho_2)h_{fg}} \right]^{1/4}$$

$$\mathscr{u}_1(x,y) \equiv Uu_1(x,y) = \frac{g(\rho_1-\rho_2)\Delta_N^2}{\mu_1}\left[\frac{\mathscr{y}}{\Delta_N} - \frac{1}{2}\left(\frac{\mathscr{y}}{\Delta_N}\right)^2 \right]$$

$$\theta_1(x,y) = \theta_w + \frac{\theta_s - \theta_w}{\delta} y$$

$$\bar{u}_1(x) \equiv \frac{1}{\Delta}\int_0^{\Delta} u_1\, dy = \frac{g(\rho_1-\rho_2)[\Delta_N(x)]^2}{3\mu_1}$$

$$\mathrm{Re}_1(x) \equiv \frac{\rho_1 g(\rho_1-\rho_2)[\Delta_N(x)]^2 x}{3\mu_1} \text{ and}$$

$$\mathrm{Re}_\delta(x) \equiv \frac{4\rho_1 U \Delta_N(x)}{\mu_1} \tag{14}$$

3 Computational Approach

Most of the details of the 2D steady/unsteady approach are the same as described in Narain et al. [3], Liang et al. [4], and Liang [5]. However, unlike the internal condensing flows considered in the earlier papers, the external condensing flow of this paper employs a different computational approach for the implementation of the pressure boundary condition described in Eq. (9). Since the boundary conditions that need to be imposed along lines AB, BC, and CD in Fig. 1 are much like prescribing the shear and pressure on the interface, the "tau-p" approach for the interface (see "tau-p" method described in Liang [5], Narain et al. [3], and Yu [21])—instead of other available approaches [22]—was adapted to satisfy the boundary conditions in Eq. (9).

The solutions' convergence in the interior of each phase, grid independence, and satisfaction of interface and boundary conditions are better (i.e., within 5%—see a representative case in Table 2) than what were reported (within 7% on average) in [3–5]. On any interface with propagating waves, the critical and difficult to satisfy requirement is Eq. (7)—the requirement of the equality of three differently computed/obtained values of interfacial mass flux (this is known to be difficult for the more general interface capturing techniques such as level set [23] or Volume of Fluid [24]). However, this requirement is met by the interface tracking approach employed in this paper (see Table 2). As shown in [3,4], one of the interface conditions [viz. $\dot{m}_{LK}=\dot{m}_{\mathrm{Energy}}$ in Eq. (7)] yields the interface tracking equation that is used in this paper. This equation is of the hyperbolic form:

$$\frac{\partial \delta}{\partial t} + \bar{u}(x,t)\frac{\partial \delta}{\partial x} = \bar{v}(x,t) \tag{15}$$

where the characteristic speed is $\bar{u} \equiv u_1^{\mathrm{i}} + \{\mathrm{Ja}/(\mathrm{Re}_1\,\mathrm{Pr}_1)\}\partial\theta_1/\partial x|^i$ and the forcing function is $\bar{v} \equiv v_1^{\mathrm{i}} + \{\mathrm{Ja}/(\mathrm{Re}_1\,\mathrm{Pr}_1)\}\partial\theta_1/\partial y|^i$.The spatial and temporal grid spacings and total lengths impose a restriction on wavelength λ and frequency f that can be adequately resolved. If the maximum spacing of the grid in the x direction is Δx_m and its total length is x_e while the total time duration is t_e and is divided in equal intervals of duration Δt; the restrictions imposed by Nyquist criteria [25] are well satisfied for $\lambda \geqslant 4\Delta x_m$ and $f \leqslant (4\Delta t)^{-1}$ and the restrictions imposed by the domain lengths are well satisfied for $\lambda \leqslant x_e/2$ and $f \geqslant 2/t_e$. The initial ($t=0$) spatial and temporal grids are defined by $(n_i \times n_j \times n_t)$, where n_i is the total number of initial grid points along x, n_j is the total number of initial grid points along y (0 to 1), and n_t is number of time steps with equal intervals (Δt). Typical values of n_i (and n_j) used were 30–40 (and 50–70) for typical maximum values of x (and y) of 50 (and 1). Attainable values of n_t depend on n_i, n_j, Δt, and the available computer memory for the storage of flow variables. For the cases reported here, typical maximum $n_t \times \Delta t$ (=t) values are in the range from 30×5 (=150) to 36×7.5 (=270).

Table 1 Specification of a flow situation involving saturated R-113 (ASHRAE [26])

p_o (kPa)	$T_s(p_o)$ (°C)	ΔT (°C)	ρ_2/ρ_1	μ_2/μ_1	We	Pr_1
108.85	49.5	5	0.005	0.020	67.9	7.3

4 Computational Results

4.1 Simulation Results for the Steady Problem. The classical Nusselt solution [1] was improvised by Rohsenow et al. [6] to account for the effects of the neglected convection term in the energy equation. Subsequently, Sparrow and Gregg [7] and Koh et al. [9] accounted for the effects of convection and inertia terms within the framework of the boundary layer and small slope approximations ($\partial/\partial x \ll \partial/\partial y$ and $\delta'^2 \ll 1$) of the governing equations.

For a specific case (see Table 1 and [26]), Figure 2(*a*) demonstrates not only the ability of our computational approach to solve the problem as posed by the Nusselt formulation [1] but, also, to solve the full steady problem without the Nusselt approximations. Since a significant amount of parametric study has already been done (see [7,9], etc.) for this problem, no parametric study has been done here. This is because this paper limits itself to a qualitative understanding of the steady base flow and has a greater focus on an understanding of the superimposed wave effects.

In Fig. 2(*a*) and its inset, for the conditions described in Table 1, "Curve 1" represents the classical analytical solution of Nusselt plotted as $\delta \equiv \Delta_N/Y_c$ against $x \equiv x/Y_c$, where Δ_N is defined in Eq. (14). "Curve 2" represents the solution under all Nusselt approximations except one—namely, in the interior equations, "$\partial/\partial x$" terms have been retained. "Curve 3" is for the case which retains the negligible vapor viscosity and negligible vapor motion assumptions (resulting in $\partial u_1/\partial y|^i=0$ and $\pi_2^i=0$) but does not neglect liquid inertia and convection. "Curve 4" is for the full problem—discussed below for "Curve 5"—except that the surface tension term on the right side of Eq. (3) has been dropped. Curve 5 is for the full steady problem posed by Eqs. (A1)–(A4) under interface conditions (2)–(8) and boundary conditions (9) and (10). The effects of the presence or absence of surface tension, as shown in Figs. 2(*c*) and 2(*e*), are negligible on the motion of the vapor but are noticeable on the interfacial values of the pressures

Table 2 Representative interfacial values of nondimensional variables show satisfaction of *all* interface conditions (for flow exposed to initial disturbance with ε=0.7 and λ_o=15) because appropriate contiguous columns are nearly equal to one another—as required by Eqs. (2)–(4), (7), and (8)

x	$\dot{m}_{LK}$	$\dot{m}_{VK}$	$\dot{m}_{\mathrm{Energy}}$	π_1^i	$\rho_2/\rho_1\pi_2^i$+terms	u_1^i	u_2^i	τ_1^i	τ_2^i	θ_1^i	θ_2^i
4	5.37E−05	5.33E−05	5.34E−05	1.86E−04	1.86E−04	1.15E−02	1.15E−02	0.009621	0.009621	64.53	64.53
8	3.55E−05	3.52E−05	3.53E−05	−2.22E−06	−2.22E−06	2.96E−02	2.96E−02	0.013676	0.013676	64.53	64.53
12	3.09E−05	3.07E−05	3.05E−05	−2.00E−06	−2.00E−06	4.29E−02	4.29E−02	0.005415	0.005415	64.53	64.53
16	2.77E−05	2.73E−05	2.74E−05	9.88E−07	9.88E−07	5.36E−02	5.36E−02	0.030117	0.030117	64.53	64.53
20	2.33E−05	2.31E−05	2.35E−05	−1.64E−06	−1.64E−06	6.76E−02	6.76E−02	0.004087	0.004087	64.53	64.42
24	2.41E−05	2.41E−05	2.46E−05	5.57E−07	5.57E−07	6.34E−02	6.34E−02	0.011717	0.011717	64.53	64.53

Note: terms$=-\frac{1}{\mathrm{We}}\left(\frac{\delta_{xx}}{[1+\delta_x^2]^{3/2}}\right)+\dot{m}^2\left(\frac{\rho_1}{\rho_2}-1\right)$.

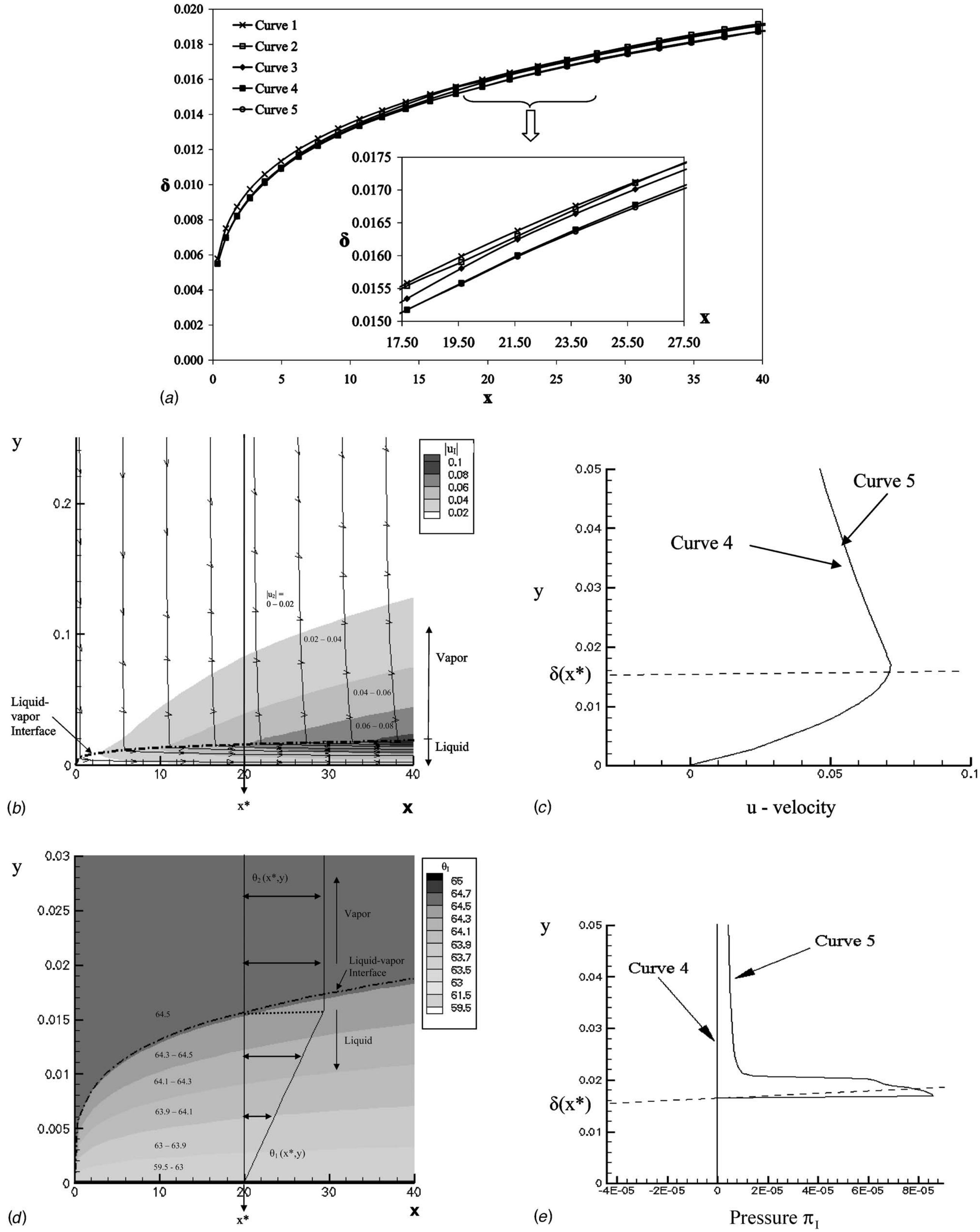

Fig. 2 (*a*) For the case of R-113 (see Table 1) experiencing film condensation on a vertical plate, the figure above shows steady film thickness values under different approximations. Here, $x_c = X_c/Y_c = 50$ and $c = Y_c/\Delta_N(X_c) = 47$. (*b*) For the case of R-113 (see Table 1) experiencing film condensation on a vertical plate, the figure above shows the streamline pattern and contour zones depicting a range of $|u_I|$ values. (*c*) For Curves 4 and 5 of the base flow in (*a*), the figure above shows the $u(x^*, y)$ versus y for $x^* = 20$. (*d*) For the case of R-113 (see Table 1) experiencing film condensation on a vertical plate, the figure above shows the contour zones for temperature and a representative plot of $\theta_I(x^*, y)$ for $x^* = 20$. (*e*) For Curves 4 and 5 of the base flow in (*a*), the figure above shows the $\pi_I(x^*, y)$ versus y for $x^* = 20$.

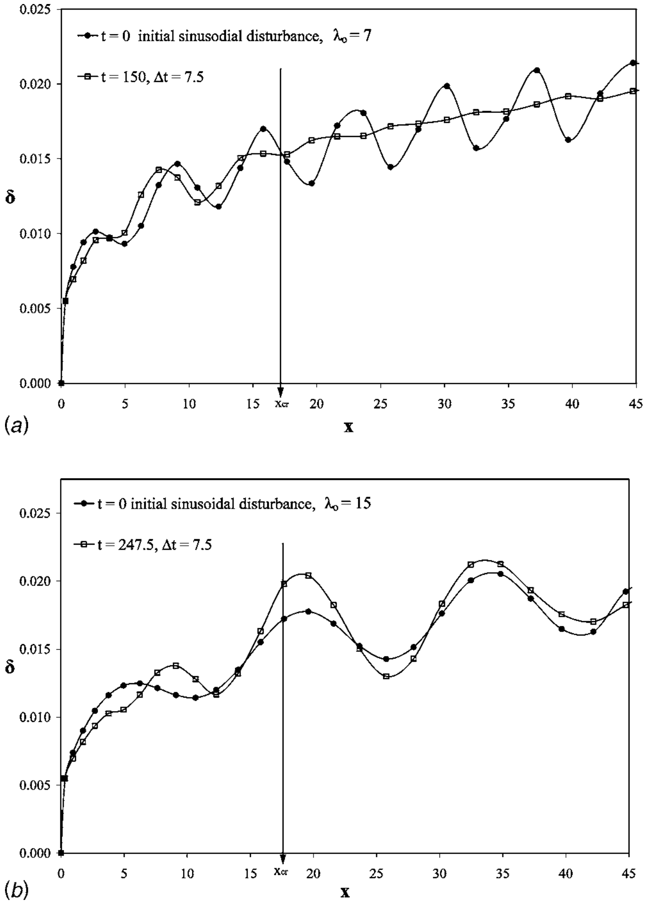

Fig. 3 (*a*) For the base flow in Fig. 2(*a*), the figure above shows the stable response (Δt=7.5, t=150) of the film thickness $\delta(x,t)$ as a result of an initial disturbance $\delta(x,0)=\delta_{\text{steady}}(x)\;[1+\varepsilon\delta'(x,0)]$, where $\delta'(x,0)\equiv\sin(2\pi x/\lambda_o)$, ε=0.15 and λ_o=7. (*b*) For the base flow in Fig. 2(*a*), the figure above shows the unstable response (Δt=7.5, t=247.5) of the film thickness $\delta(x,t)$ as a result of an initial disturbance $\delta(x,0)=\delta_{\text{steady}}(x)\;[1+\varepsilon\delta'(x,0)]$, where $\delta'(x,0)\equiv\sin(2\pi x/\lambda_o)$, ε=0.15 and λ_o=15.

π_2^i.

Generally, for all the cases considered here, the Jacob number (Ja) is small and hence all predictions of $\delta(x)$ are within 2.5% of the Nusselt solution.

4.2 Simulation Results for the Unsteady Problem.

4.2.1 Nonlinear Stability and the Effects of Initial Disturbances. The stable response of the flow in Fig. 2(*a*) to an initial sinusoidal disturbance of wavelength $\lambda=7$ is shown in Fig. 3(*a*). Here, by stability, it is meant that as waves travel forward to downstream locations, the amplitudes of the waves diminish—with respect to the initial amplitude. Similarly, by instability, it is meant that as waves travel forward to downstream locations, the amplitudes of the waves increase and become significantly larger than the initial amplitudes. Figure 3(*b*) shows an unstable response of the flow in Fig. 2(*a*) to an initial sinusoidal disturbance of wavelength $\lambda=15$. Clearly, in Figs. 3(*a*) and 3(*b*), the stability/instability phenomena manifests only after a certain downstream distance marked by $x=x_{\text{cr}}$. As indicated by the dual labeling of the x axis in Fig. 4, for any given flow, there is a one to one correspondence between $\text{Re}_\delta(x)$ and $\text{Re}_1(x)$, and, therefore, between $\text{Re}_\delta|_{\text{cr}}$ and $\text{Re}_1|_{\text{cr}}$ where $\text{Re}_\delta|_{\text{cr}}\equiv\text{Re}_\delta(x=x_{\text{cr}})$.

Figure 4 shows the general response, at $t=247.5$ of the flow in Fig. 2(*a*) to initial disturbances of various wavelengths—viz. λ =5, 9, 15, and 23. Generally, for $\lambda<\lambda_{\text{cr}}$ (here, $\lambda_{\text{cr}}\cong 11.5$), the response is stable and for $\lambda>\lambda_{\text{cr}}$, the response is unstable. The larger wavelength waves are clearly manifested for $x>x_{\text{cr}}\approx 18$ (i.e., $\text{Re}_1(x)>\text{Re}_1|_{\text{cr}}=7$ or, equivalently, $\text{Re}_\delta>\text{Re}_\delta|_{\text{cr}}\approx 28$).

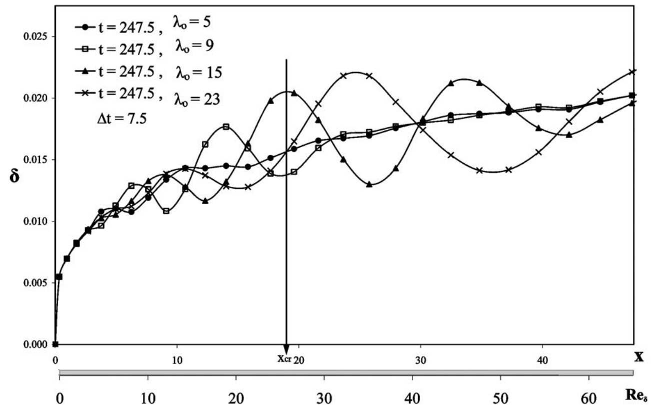

Fig. 4 For the base flow in Fig. 2(*a*), the figure above shows the stable and unstable response (Δt=7.5, t=247.5) of the film thickness $\delta(x,t)$ as a result of an initial disturbance $\delta(x,0)=\delta_{\text{steady}}(x)\;[1+\varepsilon\delta'(x,0)]$, where $\delta'(x,0)\equiv\sin(2\pi x/\lambda_o)$, ε=0.15 and λ_o=5, 9, 15, and 23

4.2.2 Effects of Surface Tension. The above described instability mechanisms—of the Tollmien-Schlichting [16] type—are only mildly affected by surface tension. Figure 5 shows that the waves are gravity dominated and surface tension effects are negligible. For the flow considered in Fig. 5, cases $\sigma=\sigma^*$ and $\sigma=2.5\sigma^*$, when compared to the $\sigma=0$ case, indicate that surface tension only slightly assists in steepening the front of the wave.

4.2.3 Computed Values of $\text{Re}_\delta|_{\text{cr}}$. A compilation of various experimental results (see Incropera and DeWitt [2] and Kutateladze [18]) for steam and common refrigerants have led to the commonly used estimate of $\text{Re}_\delta|_{\text{cr}}\approx 30$ and a subsequent laminar-to-turbulence transition regime that is characterized by $30\leqslant\text{Re}_\delta|_{\text{cr}}\leqslant 1800$. It is found that in the parameter set in Eq. (12), ρ_1 and μ_1, are important parameters affecting the value of $\text{Re}_\delta|_{\text{cr}}$ because of their appearance in the definition of Re_1 and in the nondimensionalization process itself (e.g., $\dot{m}\equiv\dot{\mathcal{M}}/\rho_1 U$). However, the remaining nondimensional parameters such as ρ_2/ρ_1, μ_2/μ_1, etc., are unimportant because, as shown later in Fig. 8,

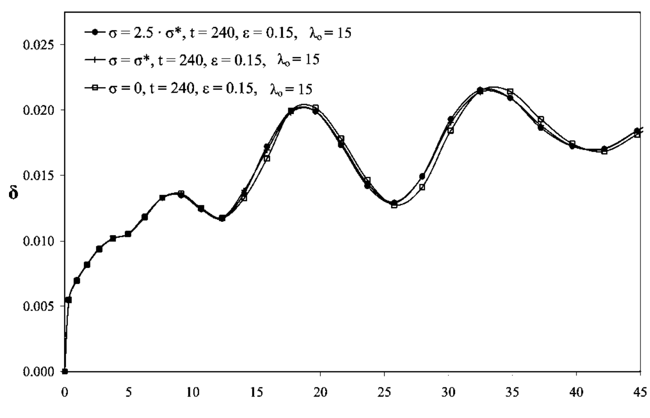

Fig. 5 For the base flow in Fig. 2(*a*), the figure above shows the effect of surface tension at the interface (Δt=7.5) on the flow exposed to initial disturbance $\delta(x,0)=\delta_{\text{steady}}(x)$ [1 $+\varepsilon\delta'(x,0)$], where $\delta'(x,0)\equiv\sin(2\pi x/\lambda_o)$, ε=0.15 and λ_o=15

Table 3 Effects of changes in $\Delta\mathcal{T}$

$\Delta\mathcal{T}$	x_{cr}	Re_δ
5	19.6	27.72
10	10.7	29.54
15	7.64	31.15
20	6.25	33.27

Note: All fluids considered here have $\rho_2/\rho_1=0.00525$, $\mu_2/\mu_1=0.0289$, We $=402.133$, and $Pr_1=7.223$.

Table 5 Effects of changing ρ_1 without significantly changing μ_1

ρ_1	μ_1	x_{cr}	Re_δ
2262	5.19E−03	15.8	28.91
1885	5.19E−03	17.4	28.35
1508	5.19E−03	19.6	27.72
1206.4	5.19E−03	19.6	24.77
1005.3	5.19E−03	17.77	22.6

Note: All fluids considered here have $\rho_2/\rho_1=0.00525$, $\mu_2/\mu_1=0.0289$, We $=402.133$, and $Pr_1=7.223$.

vapor motion does not significantly influence the wave phenomena. In addition, Table 3 shows that effects of changes in $\Delta\mathcal{T}$ are small on the values of $Re_\delta|_{cr}$ but not on x_{cr}.

Since, for common fluids, an increase in ρ_1 typically accompanies an increase in μ_1, typical changes in the kinematic viscosity ν_1 ($\equiv\mu_1/\rho_1$) values for nonmetallic vapors are limited. For this reason, as shown in Table 4, the changes in $Re_\delta|_{cr}$ with the changes in the fluid are not much and $Re_\delta|_{cr}$ remains in the 27–35 range. This justifies the continued use of the estimate $Re_\delta|_{cr}\approx 30$. However, for uncommon or specially designed fluids, one may be able to change ρ_1 without significantly changing μ_1 (Table 5) or change μ_1 without significantly changing ρ_1 (see Table 6). Under these special conditions, one can expect a more significant departure from "30" in the estimated value of $Re_\delta|_{cr}$ (e.g., in Table 6, one finds a case for which $Re_\delta|_{cr}\approx 9$).

4.2.4 Comparison of Exact Nonlinear Stability Analyses Results Presented Here With the Known Linearized Stability Results. Linearized stability analyses and associated results by Unsal and Thomas [14] and Spindler [15] for the Nusselt solution are available in the literature. However their results, though mutually compatible, are not compatible with the above described experimental estimates of $Re_\delta|_{cr}\approx 30$. Subsequent attempts at nonlinear analysis for this problem (see, e.g., Unsal and Thomas [17]) indicate the partially correct view that the instabilities predicted by linear analyses are not going to work and the problem needs some sort of non-linear analysis.

To facilitate a comparison with the known results, we present here, for the first time, the nearly exact nonlinear stability analyses and associated results. It should be noted that the predictions of the time dependent disturbances $\delta'(x,\tau)=\delta(x,t)-\delta_{steady}(x)$ in Figs. 3 and 4, associated with an initial nonzero disturbance $\delta'(x,0)$, are obtained by nearly exact nonlinear simulations (see Table 2 for representative satisfaction of all the interface conditions) and, therefore, these simulations are capable of providing good results from the point of view of both linear and nonlinear stability analyses. The initial disturbances in Figs. 3 and 4 are sinusoidal in nature and are given by the relation:

$$\delta'(x,0)=\varepsilon\cos\theta(x,0)\equiv\varepsilon\cos\left\{\frac{2\pi}{\lambda_o}(x-x_o^*)\right\}, \tag{16}$$

over a suitable range of x values with $\varepsilon>0$ and $x=x_o^*$ being a location where the phase angle $\theta(x,0)$ corresponds to a positive peak and is defined to be zero.

The time evolution $\delta'(x,t)$ of the initial disturbance in Eq. (16) can be characterized by a sinusoidal Fourier component—associated with the disturbance in Eq. (16)—and is given as:

$$\delta'(\mathbf{x},t)=a(t)\cdot\cos\theta(x,t) \tag{17}$$

However the linear and nonlinear stability analyses of condensing flow in the literature [14–17] and other air-water free-surface flows (see [27]) make the common, but restrictive, assumption that Eq. (17) can have a special simplified form, viz.

$$\delta'(x,t)=\mathrm{Re}\{\varepsilon\exp[\mathbf{i}\alpha\cdot(x-Ct)]\} \tag{18}$$

where $\alpha\equiv 2\pi/\lambda_0$ is a wave number (with λ_0 being the constant wavelength) independent of x, "$\mathbf{i}$" is the complex number $\sqrt{-1}$, and $C\equiv C_r+\mathbf{i}\cdot C_i$ is a complex number dependent only on wavelength λ_0 (or wave number α). This means that the popular analyses restrict the amplitude and phase-angle variations in Eq. (17) to:

$$a(t)=\varepsilon\exp(\alpha C_i t)\text{ and}$$

$$\theta(x,t)\equiv\alpha(x-C_r t) \tag{19}$$

The restriction in Eq. (19) is particularly severe for free surface problems (such as this problem and other air/water and evaporating flow free-surface problems) because, as shown in Eq. (27) of Narain et al. [3], the equation governing $\delta'(x,t)$ is given by:

$$\frac{\partial\delta'}{\partial t}+\bar{u}\frac{\partial\delta'}{\partial x}=\bar{\bar{v}} \tag{20}$$

where $\bar{\bar{v}}(x,t)\equiv\bar{v}(x,t)-\bar{v}_{steady}(x)-\{\bar{u}-\bar{u}_{steady}(x)\}d\delta_{steady}/dx$, $\bar{v}(x,t)\equiv v_1^i+\mathrm{Ja}/\mathrm{Re}_1\mathrm{Pr}_1(\partial\theta_1/\partial y|^i)$, as per its definition in Eq. 27 of [3].

As a result of the above, it is easy to see that waves travel along a family of characteristics curves $x=x_c(t)$, where $x_c(t)$ satisfies Eq. (25) of [3]. That is:

$$\frac{dx_c}{dt}=\bar{u}[x_c(t),t]$$

$$x_c(0)=x^*\text{ or }x_c(t^*)=0 \tag{21}$$

where x^* is any given value of $x^*>0$ and t^* is any given time $t>0$. For the no disturbance $[\bar{u}(x,t)\cong\bar{u}_{steady}]$ and large disturbance

Table 4 Effects of changes in viscosity ($\nu_1=\mu_1/\rho_1$)

ρ_1	μ_1	$\nu_1=\mu_1/\rho_1$	Fluid name for same ν_1	x_{cr}	Re_δ
1225	0.000199	1.62204E−07	R 12	5	31.93
989.4	0.000577	5.83485E−07	Water	20	25.2
1508.8	0.000519	3.44168E−07	R 113	19.6	27.72

Note: All fluids considered here have $\rho_2/\rho_1=0.00525$, $\mu_2/\mu_1=0.0289$, We $=402.133$, and $Pr_1=7.223$.

Table 6 Effects of changing μ_1 without significantly changing ρ_1

ρ_1	μ_1	x_{cr}	Re_δ
1508.8	1.04E−02	14	9.06
1508.8	7.79E−03	15.8	14.22
1508.8	5.19E−03	19.6	27.72
1508.8	3.46E−03	12.3	32.5
1508.8	2.60E−03	8.5	35.22

Note: All fluids considered here have $\rho_2/\rho_1=0.00525$, $\mu_2/\mu_1=0.0289$, We $=402.133$, and $Pr_1=7.223$.

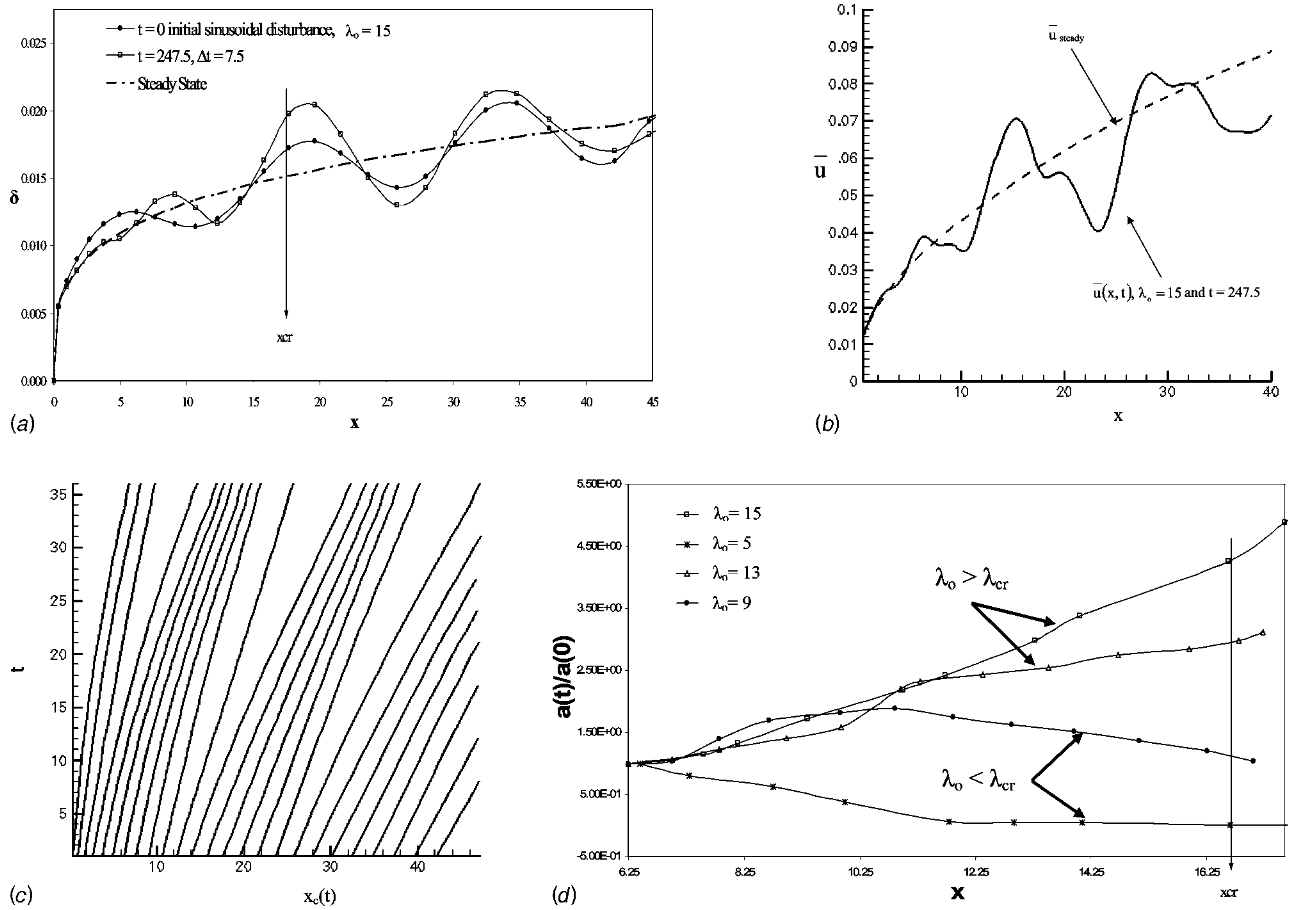

Fig. 6 (*a*) For the base flow in Fig. 2(*a*) and initial disturbances defined in Fig. 3, the figure above shows the unstable response (Δt=7.5, t=247.5), for $\lambda_o > \lambda_{cr}$, of the film thickness $\delta(x,t)$ as a result of an initial disturbance $\delta(x,0) = \delta_{steady}(x)\ [1+\varepsilon\delta'(x,0)]$, where ε=0.15 and λ_o=15. (*b*) For the case shown in (*a*), the figure above shows the values of characteristic speed $\bar{u}$ (steady value at t=0 and disturbed value at t=247.5) as function of x. (*c*) For the case shown in (*a*), the figure above shows the characteristic curves found by solving Eq. (21) through a fourth-order Runge-Kutta method. (*d*) For the cases shown in (*a*)–(*c*), the figure above shows values of $a(t)/a(0)$ for different values of initial disturbance wavelength λ_o for $x_c(t)$=6.65.

cases shown in Fig. 6(*a*), representative plots of $\bar{u}(x,t)$ are shown in Fig. 6(*b*). The linearized stability analyses assumption leading to Eq. (19) is $\bar{u}(x,t) = C_r(\lambda_0)$, where λ_0 is independent of x. The plots in Fig. 6(*b*) clearly indicate that $\bar{u}(x,t) \neq C_r(\lambda_0)$ and hence this linearized stability assumption is not appropriate. Furthermore, this assumption implies that the characteristics governing the problem are a set of *parallel* straight lines $[x_c = x_c(0) + C_r(\lambda_0)t]$. However, a fourth-order Runge-Kutta solution of Eq. (21) for $\bar{u} = \bar{u}_{steady}$ or $\bar{u}(x,t)$ leads to a set of characteristics whose slopes either change gradually with x (this is the case when $\bar{u} = \bar{u}_{steady}$) or have some superimposed oscillations on these gradually varying slopes [as shown for, $\bar{u} = \bar{u}(x,t)$, in Fig. 6(*b*)]. The characteristics associated with $\bar{u} = \bar{u}(x,t)$ in Fig. 6(*b*) are shown in Fig. 6(*c*). Clearly, the actual characteristics do not agree with the linearized stability assumption of them being a set of parallel straight lines.

In fact, with $\delta'(x,0)$ given by Eq. (16), it is easily seen that the characteristics speed $\bar{u}$ in Eq. (21) is also the phase-speed and waves traveling along the characteristics have a constant phase-angle $\theta(x,t)$, provided $\theta(x,t)$ is given by:

$$\theta(x,t) = \frac{2\pi}{\lambda_o}\left\{ x - x_o^* - \int_0^t \bar{u}[x_c(\tau),\tau]\cdot d\tau \right\} \tag{22}$$

where $x_c(\tau)$ is the characteristic $(0 \leq \tau \leq t)$ which, at time t, passes through the point x and thus satisfies $d\theta/dt = 0$ along a characteristic $x = x_c(t)$. Also, Eq. (22) is compatible with the correct phase angle associated with the initial (at t=0) disturbance in Eq. (16). Therefore, all along $x_c(\tau)$ $(0 \leq \tau \leq 0)$, we have $\theta(x,t) = \theta[x_c(\tau),\tau] = \theta[x_c(0),0] = 2\pi/\lambda_o[x_c(0) - x_o^*]$=constant.

Substitution of Eq. (22) in the definition of local wavelength $\lambda(x,t) \equiv 2\pi[\partial\theta/\partial x]^{-1}$ and local time-period $T(x,t) \equiv -2\pi[\partial\theta/\partial t]^{-1}$ (see Eq. 1.28 in [28]) imply nonconstant wavelengths (unlike the assumption in linear stability analyses) and frequencies (or time periods T) given by:

$$\lambda(x,t) = \lambda_o\left[1 - \int_0^t \frac{\partial\bar{u}}{\partial x}[x_c(\tau),\tau]d\tau\right]^{-1}$$

$$\text{and } T(x,t) = \lambda(x,t)/\bar{u}(x,t) \tag{23}$$

Also, substitution of Eq. (17) [with $\theta(x,t)$ given by Eq. (22)] in to the governing equations [Eqs. (20) and (21)] imply that, along the characteristics, the amplitude $a(t)$ grows according to the equation:

$$\frac{da}{dt} = \frac{1}{\cos\{\theta[x_c(0),0]\}}\hat{\bar{v}} \tag{24}$$

where $\hat{\bar{v}} \equiv \bar{v}[x_c(t),t]$ is the value of $\bar{v}$ in Eq. (20) along a characteristic curve. An integration of Eq. (24) along a characteristic yields:

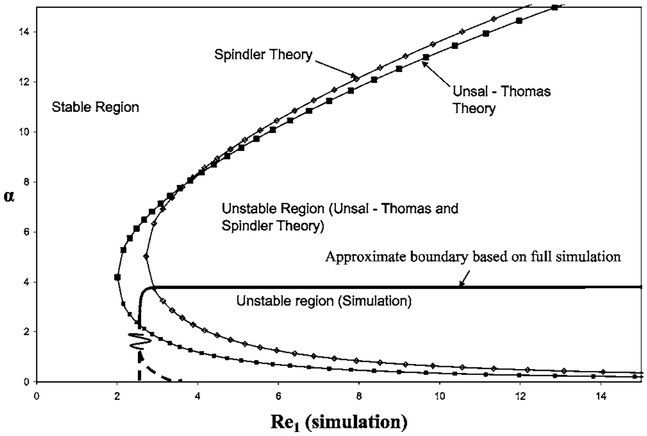

Fig. 7 Stability boundaries as obtained by Unsal and Thomas [14] and Spindler [15], and this work

$$\frac{a(t)}{a(0)} = 1 + \frac{1}{a(0)\cos\{\theta[x_c(0),0]\}} \cdot \int_0^t \hat{\bar{v}}(\tau)\cdot d\tau \qquad (25)$$

For the flow cases considered in Figs. 6(*a*)–6(*c*), a plot of "$a(t)/a(0)$" for different values of initial disturbance wavelength λ_o [see Eq. (16)], with $x_c(0)=6.65$, is shown in Fig. 6(*d*).

From Fig. 6(*d*), it is clear that the long time growth of $a(t)$ requires the full nonlinear analysis result in Eq. (25) and cannot be captured by the linearized stability assumption [14,15] of $a(t)$ being given by the exponential function in Eq. (19).

For the above reasons, for the flow considered in Figs. 6(*a*)–6(*d*), the simulation-based approximate stability boundary depicted in Fig. 7 is far more trustworthy (it is compatible with the experimental estimate on $\mathrm{Re}_\delta|_{\mathrm{cr}} \cong 30$) than the Unsal [14] and Spindler [15] results, based on the inappropriate assumptions in Eqs. (18) and (19).

It should be further noted that the nonlinear instability mechanisms illustrated by the full nonlinear solutions in Fig. 4—besides being in agreement with experiments regarding $\mathrm{Re}_\delta|_{\mathrm{cr}} \approx 30$—also show two other regularities. These regularities are: (i) As shown in Fig. 8 and its caption, the vapor motion or its fluctuations do not play a significant role in the evolution of gravity dominated waves, and (ii) the results in Fig. 5 indicate negligible impact of surface tension and this is consistent with experimental results but not with the linearized stability theory's result of a strong dependence of x_{cr} on the presence or absence of surface tension ⟨see Eq. (32) in [14] that states $x_{\mathrm{cr}} \sim \sigma^{4/11}$⟩.

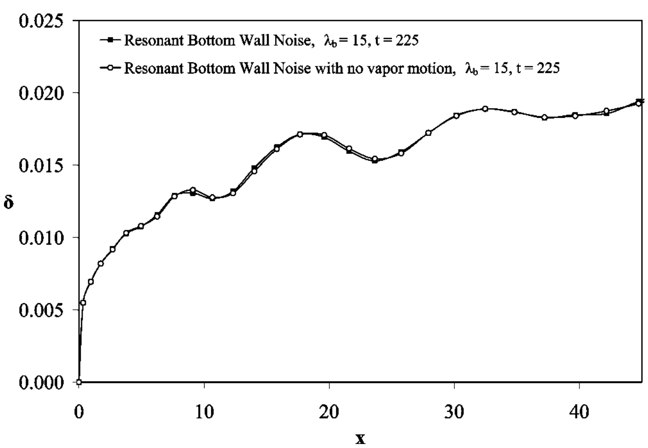

Fig. 8 Result showing waves while accounting for vapor motion and its fluctuations and, also, while neglecting vapor motion and its fluctuations (by not incorporating vapor domain calculations in the simulations). Here, $\Delta t=7.5$ and $\varepsilon_b=0.15$ *E*-05.

4.2.5 Different Wave Mechanisms in Different Zones. As marked in Fig. 4, for $x<x_{\mathrm{cr}}$, the initial disturbances may persist but the zone is considered stable because the growth of the waves is considered small. However, at longer lengths in Fig. 6(*d*), there is a loss of stability, that is, amplitudes for $\lambda_o>\lambda_{\mathrm{cr}}$ are eventually sufficiently large. The largeness of amplitude $a(t)$ is defined here to mean that, for $x>x_{\mathrm{cr}}$, $a(t)/a(0)\geqslant 2.5$ at large t and, at the same time, the peaks of the resulting disturbances are off by more than 15% of the initial undisturbed film thickness values at the current locations of the waves (see Fig. 4). In the above definition of x_{cr}, the large amplitude waves at $x>x_{\mathrm{cr}}$ (see Fig. 4) arise from initial disturbances at $x\sim 0$, where their amplitudes are sufficiently small (less than 10% of the small steady film thickness at $x\sim 0$). Another feature of x_{cr} being defined this way is that for $\lambda_o<\lambda_{\mathrm{cr}}$, the amplitude ratio $a(t)/a(0)$ is eventually less than 1,0 [i.e., $a(t)/a(0)<1$] at large t. Under the above definition, the longer length flows lose stability for $\mathrm{Re}_\delta \geqslant \mathrm{Re}_\delta|_{\mathrm{cr}} \approx 30$.

The wall noise is assumed to be a superposition of standing waves of the form given by:

$$v_1(x,0,t) = \varepsilon_b \sin(2\pi x/\lambda_b)\sin(2\pi t/T_b) \qquad (26)$$

As shown in [3], one expects a resonance condition to hold if the time period of oscillations T_b in the wall noise of Eq. (26) is such that the forward travelling component of the standing noise has approximately the same phase-speed as $\bar{u}(x,t)$ (which is nearly equal to $\bar{u}_{\mathrm{steady}}$ for small amplitude interfacial waves). This means, for resonance with large amplitude waves, $T_b=T_b(x,t)$ must satisfy:

$$\frac{\lambda_b}{T_b(x,t)} = \bar{u}(x,t) \cong \bar{u}(x,t-\Delta t) \qquad (27)$$

or $T_b=T_b(x)$ must satisfy:

$$\frac{\lambda_b}{T_b(x)} = \bar{u}_{\mathrm{steady}}(x) \qquad (28)$$

For nonresonant single frequency (T_b=constant) wall noise, as shown in Figs. 9(*a*) and 9(*b*), depending on the value of T_b, one may have either a negligible (if T_b is nowhere in the resonant range) or a constructive (if T_b is somewhere in the resonant range) interference between wall noise and intrinsic waves. As shown in Fig. 10(*a*), for the unstable $\lambda_b=15>\lambda_{\mathrm{cr}}$ case (where λ_{cr} is same as the one obtained from the earlier initial disturbance analysis), the resonant wall noise [in the sense of Eqs. (27) and (28)] interacts with the intrinsic waves and sustains a large amplitude travelling wave. Differently, but interestingly, as shown in Fig. 10(*b*), for the damped or stable $\lambda_b=5<\lambda_{\mathrm{cr}}$ case, the resonant bottom wall noise governed by Eq. (28) interacts with the intrinsic waves and sustains a travelling wave which "beats" in the sense that the noises are alternately damped over a period of time and then regained over a subsequent period of time.

The above shows that wave effects will, in general, be present. They may be intrinsic in the absence of wall noise (i.e., due to initial disturbances alone) or they may be interactive in the presence of wall noise. Furthermore, the extent of the wave effects on heat transfer rates and interfacial shear will, in general, remain nondeterministic unless, experimentally, one can use wall noise actuation to have a well-defined, enhanced, or diminished form of wave effects.

4.2.6 Impact on the Heat Transfer Rates and Shear Stress. Effect of waves on the wall heat transfer rate and wall shear stress, for the $\lambda>\lambda_{\mathrm{cr}}$ initial disturbance case of Fig. 4, is shown in Figs. 11(*a*) and 11(*b*). This confirms the well known [2] fact that, in the presence of gravity-assisted drainage, intrinsic waves enhance

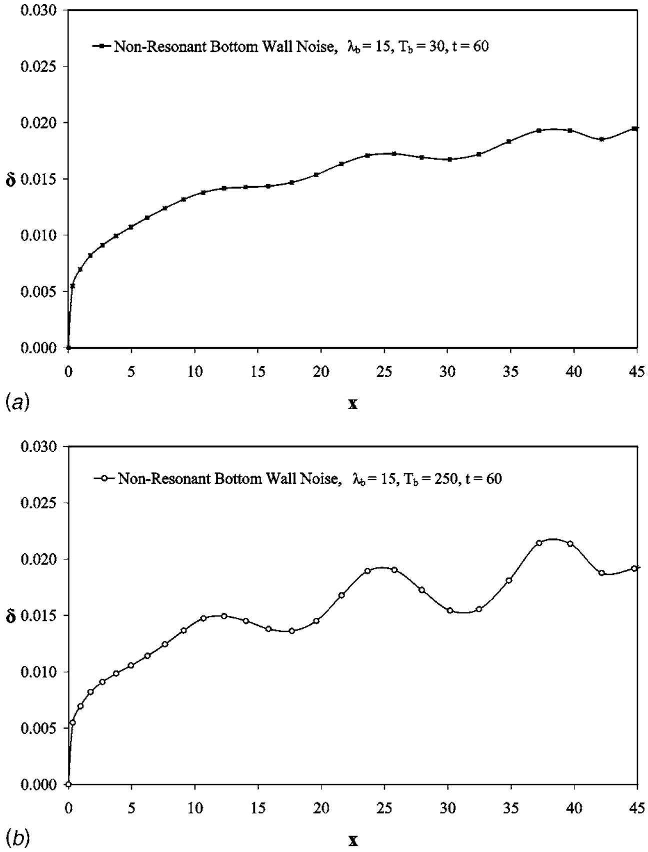

Fig. 9 (*a*) Nonresonance bottom wall noise that do not lead to growing waves. Here, Δt=7.5, ε_b=0.15 *E*-05, and T_b=30. (*b*) Nonresonance bottom wall noise that lead to growing waves. Here, Δt=7.5, ε_b=0.5 *E*-05 and T_b=250.

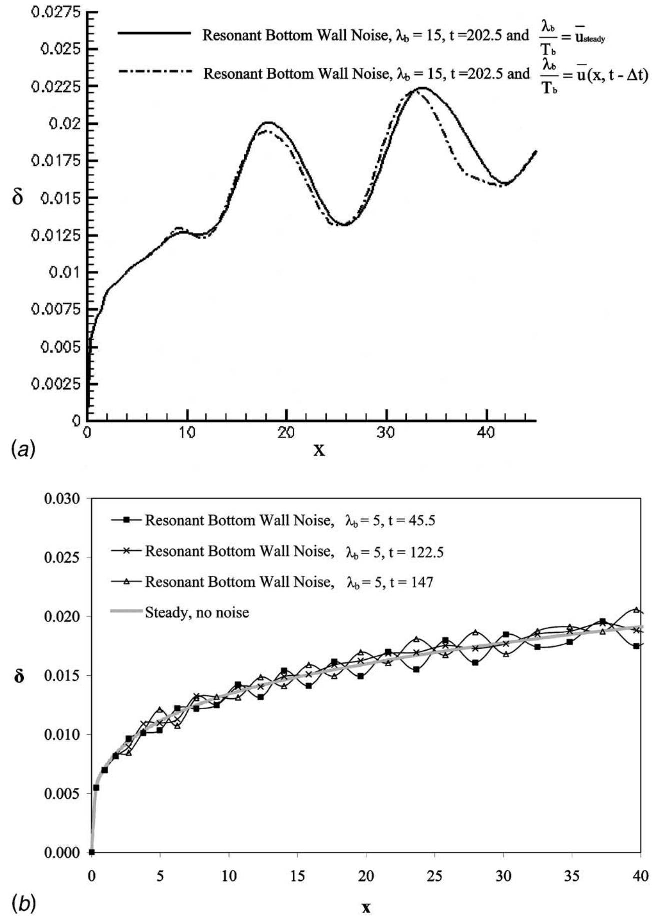

Fig. 10 (*a*) Effects of resonant noise for λ_b=15>λ_{cr} and with Δt=7.5 and ε_b=0.35 *E*-05. (*b*) Effects of resonant noise for λ_b=5<λ_{cr} and with Δt=7.5 and ε_b=0.5 *E*-05.

both of these important parameters. The extent of the heat transfer enhancements is typically found to be within the range (i.e. 1.2 times the values associated with smooth-interface heat transfer rates) suggested by empirical correlations (see [2,18]). This enhancement can be actively increased or reduced with the help of resonant or nonresonant wall noises.

5 Conclusions

- The computational approach presented here accurately solves the steady Nusselt problem and produces results in agreement with the Nusselt solution.
- The results considered thus far affirm the experimental result that instability mechanisms associated with laminar to turbulence transitions can typically be estimated to occur around $\mathrm{Re}_{\delta}|_{\mathrm{cr}} \approx 30$.
- The waves and the wave effects are quite sensitive to the presence or absence of the wall noise. This sensitivity to the frequency and wavelength spectrum of the wall noise can be exploited either to suppress or enhance the wave effects.
- As is well known for this problem, the results affirm that heat transfer rates and shear rates are significantly enhanced by the presence of waves.

Acknowledgment

This work was supported by NSF Grant No. CTS-0086988 and NASA Grant No. NNC04GB52G.

Nomenclature

X_c = distance from leading edge (BC in Fig. 1), m
Y_c = characteristics length (AB in Fig. 1), m
U = average liquid speed (Nusselt) at $x=X_c$, $g(\rho_1\text{-}\rho_2)\Delta_N^2(X_c)/3\mu_1$, m/s
(x, y, t) = physical distances (see Fig. 1) and physical time, (m, m, s)
(x, y, t) = nondimensional values of (x, y, t)
k = thermal conductivity, W/(m K)
C_p = specific heat, J/(kg K)
p = pressure, N/m^2
p_o = pressure at the inlet, N/m^2
(u, v) = values of x and y components of velocity, m/s
(u, v) = nondimensional values of u and v
T = temperature, K
ΔT = temperature difference between the vapor and the wall, K
h_{fg} = latent heat (h_g-h_f), J/kg
Ja = Jacob number, $C_{p1}\Delta T/h_{fg}$
Re_{I} = Reynolds number $\rho_{\mathrm{I}}UX_c/\mu_{\mathrm{I}}$
$\mathrm{Re}_1(x)$ = Reynolds number $\rho_1 Ux/\mu_1$
$\mathrm{Re}_\delta(x)$ = film Reynolds number $4\rho_1 U\Delta_N(x)/\mu_1$
Pr_{I} = Prandtl number $\mu_{\mathrm{I}}Cp_{\mathrm{I}}/k_{\mathrm{I}}$
Fr = Froude number U^2/gY_c
We = Weber number $\rho_1 U^2 Y_c/\sigma$
q''_w = bottom wall heat flux at any point and time, W/m^2

Greek Symbols

π = nondimensional pressure
θ = nondimensional temperature

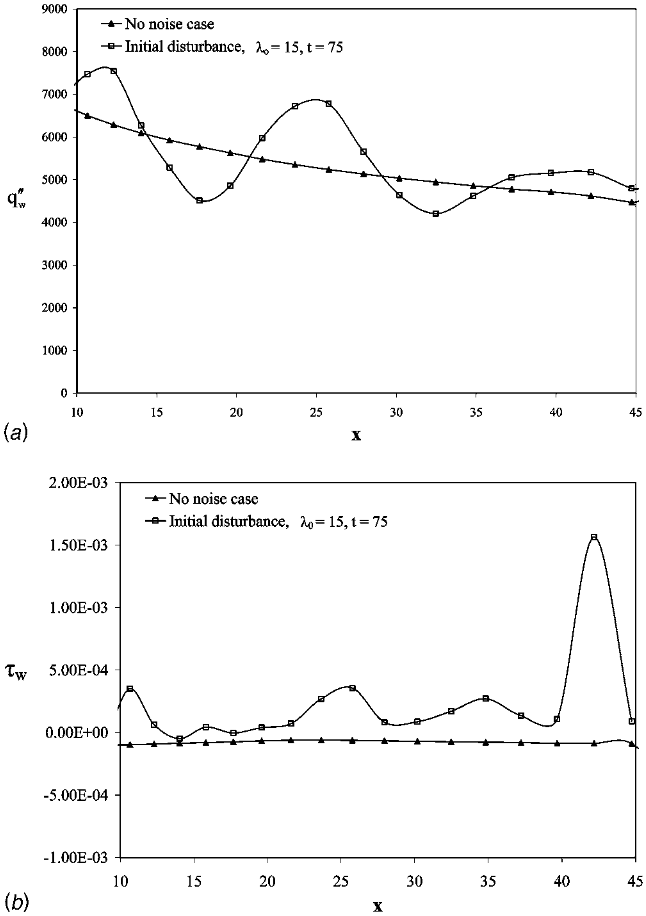

Fig. 11 (*a*) For the base flow in Fig. 2(*a*), the figure above shows the wall heat flux (W/m^2) for cases with and without initial disturbance $\delta(x,0)=\delta_{\text{steady}}(x)\ [1+\varepsilon\delta'(x,0)]$, where $\delta'(x,0)\equiv\sin(2\pi x/\lambda_o)$, $\varepsilon=0.15$, $\lambda_o=15$, and $\Delta t=7.5$. (*b*) For the base flow in Fig. 2(*a*), the figure above shows the wall shear stress for cases with and without initial disturbance $\delta(x,0)=\delta_{\text{steady}}(x)\ [1+\varepsilon\delta'(x,0)]$, where $\delta'(x,0)\equiv\sin(2\pi x/\lambda_o)$, $\varepsilon=0.15$, $\lambda_o=15$, and $\Delta t=7.5$.

ρ = density, kg/m^3
μ = viscosity, Pa s
Δ = physical value of condensate thickness, m
Δ_N = physical value of Nusselt film thickness at x, $[(4k_1\Delta T\mu_1 x)/(h_{fg}\rho_1(\rho_1-\rho_2)g)]^{1/4}$, m
δ = nondimensional value of condensate thickness
ν = kinematic viscosity μ/ρ, m$^2/s$
σ = surface tension, N/m
ε = amplitude of nondimensional disturbances representing values of $\delta'(x,0)$
ε_b = amplitude of nondimensional bottom wall vibrations sensed through $v_1(x,0,t)$
λ = nondimensional wavelength
λ_o = nondimensional wavelength for the initial disturbance $\delta'(x,0)$
α = wave number, $2\pi/\lambda$

Subscripts

I = it takes a value of 1 for liquid phase and 2 for vapor phase
s = saturation condition
w = wall
b = bottom wall

Superscripts

i = value of a variable at an interface location

Appendix

The differential forms of mass, momentum (x and y components), and energy equations in terms of nondimensional variables for flows in the interior of either of the phases ($I=1$ or 2) for this external flow are given as

$$\frac{\partial u_I}{\partial x}+\frac{\partial v_I}{\partial y}=0 \tag{A1}$$

$$\frac{\partial u_I}{\partial t}+u_I\frac{\partial u_I}{\partial x}+v_I\frac{\partial u_I}{\partial y}=-\left(\frac{\partial \pi_I}{\partial x}\right)+\mathrm{Fr}_x^{-1}+\frac{1}{\mathrm{Re}_I}\left(\frac{\partial^2 u_I}{\partial x^2}+\frac{\partial^2 u_I}{\partial y^2}\right) \tag{A2}$$

$$\frac{\partial v_I}{\partial t}+u_I\frac{\partial v_I}{\partial x}+v_I\frac{\partial v_I}{\partial y}=-\left(\frac{\partial \pi_I}{\partial y}\right)+\mathrm{Fr}_y^{-1}+\frac{1}{\mathrm{Re}_I}\left(\frac{\partial^2 v_I}{\partial x^2}+\frac{\partial^2 v_I}{\partial y^2}\right) \tag{A3}$$

$$\frac{\partial \theta_I}{\partial t}+u_I\frac{\partial \theta_I}{\partial x}+v_I\frac{\partial \theta_I}{\partial y}\approx\frac{1}{\mathrm{Re}_I\,\mathrm{Pr}_I}\left(\frac{\partial^2 \theta_I}{\partial x^2}+\frac{\partial^2 \theta_I}{\partial y^2}\right), \tag{A4}$$

where $\mathrm{Re}_1\equiv\rho_1 UY_c/\mu_1$, $\mathrm{Pr}_1\equiv\mu_1 Cp_1/k_1$, $\mathrm{Fr}_x^{-1}\equiv g_x Y_c/U^2$, and $\mathrm{Fr}_y^{-1}\equiv g_y Y_c/U^2$.

Under negligible inertia, negligible convection, and boundary layer ($\partial/\partial x\ll\partial/\partial y$) approximations for thin condensate, Nusselt formulation [1] effectively replaces, for $I=1$, (A2)–(A4) above by:

$$0\cong-\frac{\partial \pi_I}{\partial x}+\mathrm{Fr}_x^{-1}+\frac{1}{\mathrm{Re}_I}\frac{\partial^2 u_I}{\partial y^2}$$

$$0\cong-\frac{\partial \pi_I}{\partial y}+\mathrm{Fr}_y^{-1}$$

$$0\cong\frac{1}{\mathrm{Re}_I\,\mathrm{Pr}_I}\cdot\frac{\partial^2 \theta_I}{\partial y^2} \tag{A5}$$

For $I=2$, the additional Nusselt [1] approximation of negligible vapor viscosity and saturated vapor eliminates any consideration of vapor motion and vapor temperature variation for obtaining the steady liquid condensate solution. Therefore, one does not need to consider the vapor ($I=2$) Eqs. (A1)–(A4) in order to obtain the Nusselt ([1]) solution.

The term $[t]$ on the right side of Eq. (4) is given by:

$$[t]=\left\{\frac{\mu_2}{\mu_1}\frac{\partial v_2}{\partial x}\bigg|^i-\frac{\partial v_1}{\partial x}\bigg|^i\right\}+\frac{2\delta_x}{[1-\delta_x^2]}\left\{\frac{\partial u_1}{\partial x}\bigg|^i-\frac{\partial v_1}{\partial x}\bigg|^i\right\}-\frac{2\delta_x}{[1-\delta_x^2]}\frac{\mu_2}{\mu_1}\left\{\frac{\partial u_2}{\partial x}\bigg|^i-\frac{\partial v_2}{\partial y}\bigg|^i\right\} \tag{A6}$$

References

[1] Nusselt, W., 1916, Die Oberflächenkondesation des Wasserdampfes, Z. Ver. Dt. Ing., **60**(27), pp. 541–546.
[2] Incropera, F. P., and DeWitt, D. P., 1996, *Fundamentals of Heat and Mass Transfer*, 4th ed., Wiley, New York.
[3] Narain, A., Liang, Q., Yu, G., and Wang, X., 2004, "Direct Computational Simulations for Internal Condensing Flows and Results on Attainability/Stability of Steady Solutions, their Intrinsic Waviness and their Noise Sensitivity," ASME J. Appl. Mech., **71**, pp. 69–88.
[4] Liang, Q., Wang, X., and Narain, A., 2004, "Effect of Gravity, Shear, and Surface Tension in Internal Condensing Flows—Results From Direct Computational Simulations," ASME J. Heat Transfer, **126**(5), pp. 676–686.
[5] Liang, Q., 2003, "Unsteady Computational Simulations and Code Developments for a Study of Internal Film Condensation Flows Stability, Noise Sensitivity and Wavyness," Ph.D. thesis, Michigan Technological University.
[6] Rohsenow, W. M., 1956, "Heat Transfer and Temperature Distribution in Laminar Film Condensation," Trans. ASME, **78**, pp. 1645–1648.
[7] Sparrow, E. M., and Gregg, J. L., 1959, "A Boundary Layer Treatment of

Laminar Film Condensation," ASME J. Heat Transfer, **81**, pp. 13–18.
[8] Chen, M. M., 1961, "An Analytical Study of Laminar Film Condensation: Part 1—Flat Plates," ASME J. Heat Transfer, **83**, pp. 48–54.
[9] Koh, J. C. Y., Sparrow, E. M., and Hartnett, J. P., 1961, "The Tow-Phase Boundary Layer in Laminar Film Condensation," Int. J. Heat Mass Transfer, **2**, pp. 69–82.
[10] Dhir, V. K., and Lienhard, J. H., 1971, "Laminar Film Condensation on Plane and Axisymentric Bodies in Nonuniform Gravity," ASME J. Heat Transfer, **93**, pp. 97–100.
[11] Arnas, A. O., Boettner, D. D., Benson, M. J., and Van Poppel, B. P., 2004, "On the Teaching Of Condensation Heat Transfer," Proceedings of ASME-IMECE 2004, Paper No.: IMECE2004-59277, 15–19 Nov., Anaheim, CA.
[12] Miyara, A., 2001, "Flow Dynamics and Heat Transfer of Wavy Condensate Film," ASME J. Heat Transfer, **123**, pp. 492–500.
[13] Stuhlträger, E., Naridami, Y., Miyara, A., and Uehara, H., 1993, "Flow Dynamics and Heat Transfer of a Condensate Film on a Vertical Wall—I. Numerical Analysis and Flow Dynamics," Int. J. Heat Mass Transfer, **36**, pp. 1677–1686.
[14] Unsal, M., and Thomas, W. C., 1978, "Linearized Stability Analysis of Film Condensation," ASME J. Heat Transfer, **100**, pp. 629–634.
[15] Spindler, B., 1982, "Linear Stability of Liquid Films With Interfacial Phase Change," Int. J. Heat Mass Transfer, **25**, pp. 161–173.
[16] Kundu, P. K., 1990, *Fluid Mechanics*, Academic Press, New York.
[17] Unsal, M., and Thomas, W. C., 1980, "Nonlinear Stability of Film Condensation," ASME J. Heat Transfer, **102**, pp. 483–488.
[18] Kutateladze, S. S., 1963, *Fundamentals of Heat Transfer*, Academic Press, New York.
[19] Chun, K. R., and Seban, R. A., 1971, "Heat Transfer to Evaporating Liquid Films," ASME J. Heat Transfer, **93**, pp. 391–396.
[20] Delhaye, J. M., 1974, "Jump Conditions and Entropy Sources in Two-phase Systems; Local Instant Formulation," Int. J. Multiphase Flow, **1**, pp. 395–409.
[21] Yu, G., 1999, "Development of a CFD Code for Computational Simulations and Flow Physics of Annular/Stratified Film Condensation Flows," Ph.D. thesis, Michigan Technological University.
[22] *COMPACT-2D User Manual (Version 3.1)*, 1994, Innovative Research, Inc., Computational Fluid Dynamic Company, Minneapolis, MN.
[23] Sussman, M., Smereka, P., and Osher, S., 1994, "A Level Set Approach for Computing Solutions to Incompressible Two-Phase Flow," J. Comput. Phys., **114**, pp. 146–159.
[24] Hirt, C. W., and Nichols, B. D., 1981, "Volume of Fluid (VOF) Method for the Dynamics of Free Boundaries," J. Comput. Phys., **39**, pp. 201–255.
[25] Abbott, M. B., and Basco, D. R., 1997, *Computational Fluid Dynamics: An Introduction for Engineers*, Longman Science and Technol., Harlow, Essex, England.
[26] *ASHRAE Handbook*, 1985, Fundamentals SI ed., American Society of Heating, Refrigeration and Air-Conditioning Engineers, Inc., Atlanta, GA.
[27] Pierson, F. W., and Whitaker, S., 1977, "Some Theoretical and Experimental Observations of the Wave Structure of Falling Liquid Films," Ind. Eng. Chem. Fundam., **16**(4), pp. 401–408.
[28] Whitham, G. B., 1974, *Linear and Nonlinear Waves*, Wiley, New York.